The effect of nanoconfinement on the phase behavior of ethane/n-propane binary mixture: An experimental study at varying pore sizes and compositions

Keerti Vardhan Sharma[a,*], *Rami M.* Alloush[a], *Karem* Al-Garadi[a], and *Mohammad* Piri[a]

[a]Center of Innovation for Flow through Porous Media, Department of Petroleum Engineering, University of Wyoming, Laramie, Wyoming, USA, 82071

Abstract. Enhanced fluid-solid and fluid-fluid interactions due to nanoconfinement in unconventional gas reservoirs can translate to the hydrocarbon components showing different phase behaviors than those observed during the bulk phase analysis. Furthermore, desorption of fluids from nanopores during production from unconventional reservoirs results in reduced reservoir pressure, strengthening the effect of capillarity on the phase behavior of the hydrocarbons. Efforts are being made to develop and improve phase behavior models to predict the effect of confinement on phase equilibria of hydrocarbon mixtures in nanopores. Nonetheless, the scarcity of experimental data revealing the effects of factors such as pore size distribution on adsorption and desorption behaviors of the hydrocarbon components poses a major impediment to improving the accuracy of the models. This experimental study investigates the effect of confinement on the phase equilibria of binary mixtures of Ethane/n-Propane with different compositions in MCM-41 nanoporous material at three different pore sizes of 6 nm, 8 nm, and 12 nm. The condensation pressures of the mixture for these pore sizes are determined from the mass-pressure isotherms obtained during the adsorption process using a patented gravimetric apparatus. The variations in the condensation pressures with respect to pore sizes for different compositions of the binary mixture manifest the effect of capillary pressure and molar fraction on the vapor-liquid equilibrium. Furthermore, a direct proportionality with the pore size was evident from the results, which agrees with the trends available in the literature. The results also demonstrate that the relative quantities of the components play a significant role in the shifting of the phase envelopes of hydrocarbon mixtures. Additionally, the degree of selective adsorption in the nanopores decreases with an increase in the molar fraction of heavy components. This study presents a new dataset that improves the current understanding of the phase behavior of hydrocarbon mixtures in nanopores. Moreover, this investigation can be of great interest to the researchers developing phase behavior models to study vapor-liquid equilibria of the confined fluids.

1 Introduction

Hydrocarbons have been a vital part of modern human life for the past century and will continue to satiate the ever-growing global energy demand in the near future [1]. Hydrocarbons such as ethane (C_2H_6) and propane (C_3H_8) are the most significant natural organic deposits available in geological formations, along with methane [2]. In addition, they are essential for numerous industrial and domestic applications [3,4]. For example, they are used as a fuel [5-10], sources for hydrogen and methane production [11,12], solvents [13], fluids for cooling and heating in the petrochemical industry [14-16], and catalysts [17].

The bulk thermodynamic properties of pure ethane, propane, ethane/propane mixture, and their mixtures with other fluids in the gaseous or liquid states have been studied extensively [18-29]. For example, the bulk phase behaviors of ethane and propane gases were determined using statistical thermodynamic approaches for a wide range of temperatures (0 to 1,500 K) at atmospheric pressure [30]. In addition, phase behaviors of various mixtures containing ethane, propane, or both and other fluids such as Xenon [31], hydrogen [32], water [33,34], CO_2 [35,36], hydrate [37], sunflower oil [38], bitumen [39], and other hydrocarbons [40-45] have been evaluated at different conditions. However, only a few studies investigated the phase behavior characteristics of ethane and propane and their mixtures in confined spaces, which significantly differ from those observed in bulk conditions [46,47]. This difference is attributed to the effects of confinement, which are governed by intensified fluid-fluid and solid-fluid interactions. Such interactions control the

* Corresponding author: ksharma1@uwyo.edu

flow of confined fluids in porous media, resulting from altered phase behavior due to nanoconfinement.

Understanding the phase behavior of fluids in nanoconfinement is critical for several disciplines in science and engineering, such as geochemistry [48], hydrogen storage [49], catalysis [50], heat transfer [51–53], and drug delivery [54]. An example from the oil industry is shale reservoirs, where nanopores make up a significant portion of the hydrocarbon-bearing matrix compared to those of the macropores and fractures [55,56]. It is paramount to carefully characterize the confined phase behavior of hydrocarbons stored in nanopores for effective development and recovery optimization from unconventional resources such as shales [57–59].

Several researchers have made notable efforts to develop numerical models that can account for the fluid-fluid and solid-fluid interactions in confined fluid systems. Ma and Jamili [59] used the Simplified Local-Density (SLD) theory to modify the Peng-Robinson equation of state (PR-EOS) to probe the fluid-wall interactions under nanoconfinement. They calculated the density profiles as a function of pore width for ethane and propane in a 5-nm wide slit pore under conditions of 3,043 psi and 80 °C. This work was based upon the modified model (SLD-PR). The density profiles for ethane and propane were distinct from each other such that propane had higher bulk densities and adsorbed layer densities than those of ethane. In addition, ethane showed a significant difference between its adsorbed and bulk densities than that exhibited by propane. Therefore, they concluded that the confinement effects are more pronounced on lighter fluids than on heavier ones in the same pore size and at similar temperature and pressure conditions. Dong et al. [58] coupled the cubic Peng-Robinson (PR) equation of state (EOS) with the multicomponent potential theory of adsorption (MPTA) to study and model the confined behavior of pure ethane, propane, and ethane/methane and propane/methane mixtures in organic nanopores. In addition, the thermodynamic properties of ethane and propane hydrates were investigated in porous silica gels of four different pore sizes 100, 30, 15, and 6 nm [60]. Sugata and Piri developed a modified equation of state (EOS) to evaluate the thermodynamic properties of fluids under nanoconfinement. The authors combined the perturbed chain-statistical associating fluid theory (PC-SAFT) EOS with the Young-Laplace equation to account for the effect of capillary pressure in predicting the phase behavior of confined fluids [61].

Barsotti et al. [62] presented experimentally measured isotherms of pure propane in mesoporous silica MCM-41 of various pore sizes (8.08, 4.19, and 2.90 nm) over a wide range of temperatures, from 5 to 50 °C. They found that propane's capillary condensation pressure increased with an increase in temperature and pore size. In addition, the adsorption branch of the propane isotherms showed a concave shape, reflecting the effect of fluid-solid interactions. Furthermore, these isotherms followed the common capillary condensation trend, and exhibited hysteresis and the effect of supercriticality (see [62] for more details). Other studies observed that the capillary condensation of propane in crushed shale could result in significant swelling of kerogen that can in turn induce fractures and pore deformation [63,64].

Zhao and Jin [65] studied methane/propane mixture phase behavior in nanopores connected to the bulk regions (i.e., nanopores connected to macropores and natural/hydraulic fractures) using density functional theory (DFT). They determined that a two-phase region could form inside the nanopores, and its size grows with increasing pore size. However, this study employed a uniform pore size model and did not consider the effect of the pore size distribution (PSD). In another study by the same authors [66], they used the DFT and the same fluid mixture (methane/propane) to investigate the effect of PSD on capillary condensation in nanopores during constant composition expansion (CCE) and constant volume depletion (CVD) processes. They considered the impact of the interplay between nanopores and macropores/fractures, which was overlooked in other studies that focused only on the effect of the PSD [65, 67]. To this end, two different pore sizes (5 nm and 10 nm) were numerically generated, and three PSD models with varying ratios of nanopores and bulk region volumes were constructed. The simulated media represented oil-wet pores of carbon slits, while the macropores/fractures denoted the bulk region where the confinement effects did not exist. They concluded that when pressure declines (i.e., desorption of fluids), the phase transitions occur first in bulk, then in the larger pores, followed by smaller pores. In addition, the composition of the heavier component decreases in the phase transition region but increases in the other areas with no phase transition. The trend mentioned above is due to the influence of PSD, which becomes more pronounced as the pressure goes below the dew point pressure, and propane inside the nanopores can be released in this pressure region. As the proportion of the smaller pores in the system becomes larger, the confinement effect in these media becomes stronger. And the communication between the nanopores and bulk induces the accumulation of heavier components. Thus, the recovery of the heavier molecules is suppressed.

It is evident from the literature that most studies probed the confined phase behavior of fluids using numerical techniques. Only a limited number of investigations have been dedicated to experimentally probing the effects of confinement, and these have mostly used a single component and employed a narrow range of pore sizes. To the best of our knowledge, no experimental study probed the effects of composition and pore sizes on the phase behavior of the ethane/propane mixture in nanopores. In this study, we employed an advanced gravimetric technique to study the phase behavior of confined ethane/propane mixture for two different compositions in three different sizes of nanopores (7, 10.2, and 12.3 nm). The two compositions used were (M1) 46.6% and 53.4% and (M2) 37.3% and 62.7% of ethane and propane, respectively. The adsorption isotherms were measured at -18 °C.

The remainder of this paper is organized as follows. **Section 2** provides details about the materials and methods used to conduct the experiments. This section briefly discusses the specifications of the materials and fluids used as adsorbents and adsorbates, preparation of the nanoporous materials and apparatus, experimental procedure, and the data acquisition and processing techniques. The experimental results, such as adsorption isotherms for both compositions in all three pore sizes, are presented and analyzed in **Section 3**. Finally, the conclusions and final remarks are listed in **Section 4**.

2 Materials and methods

2.1 Materials and sample preparation

Three different sizes of the mesoporous silica material known as MCM-41 were acquired from Glantreo, Ltd. This material is known for its controlled pore shapes and sizes. The nanopores of MCM-41 are unconnected, cylindrical in shape, and possess a uniform pore size distribution [68]. The provider-specified pore sizes of the MCM-41 samples used in this work are 6, 8, and 12 nm. The non-local density functional theory (NLDFT) analysis was performed on these samples to determine the average pore size of the material. **Table 1** shows the pore diameters of the MCM-41 samples calculated by using the NLDFT.

Table 1: Pore diameter of various MCM-41 samples used in this study. The pore size distributions for all samples are provided in **Appendix I**.

MCM-41 samples	NLDFT Pore diameter (nm)
MCM-41 (60 A)	7
MCM-41 (80 A)	10.2
MCM-41 (120 A)	12.3

We observed a certain degree of discrepancy in the pore diameters given by the provider and those obtained through b the NLDFT calculations. The latter generated pore diameter values that were larger than those provided by the manufacturer. Samples were packed into different titanium sample holders using a standard procedure (see Ref. [62] for details). Research grade ethane and propane gases were obtained from Airgas Inc. Both gases possessed 99.8% purity. The fluid mixture was prepared in-house using a mixing setup consisting of a two-cylinder ISCO pump, a high-accuracy balance, a vacuum pump, and an accumulator.

2.2 Apparatus

A patented gravimetric nanocondensation apparatus [69] was employed to measure the adsorption isotherms. The schematic diagram of the apparatus is shown in **Figure 1**. It consisted of an environmental chamber from Thermotron, sample holders, and four Mettler Toledo mass comparators. Different samples of the nanoporous material were packed inside the sample holders, which were housed inside the environmental chamber. The chamber could operate over a wide range of subzero and high-temperature conditions and maintain the desired temperature with an accuracy of ±0.1 °C. The highly advanced XPE 505 C mass comparators possessed an accuracy of ±0.00001 g. They were located above the environmental chamber on an anti-vibration platform and suspended the sample holders inside the enclosure through thin metal wires. The changes in the mass of the adsorbed fluid were directly measured using these balances during the experiment. The apparatus allows for the measurement of four isotherms simultaneously. Other key components and configurations of the apparatus, such as pumps, pressure transducers, and different valve assemblies, are shown in **Figure 1**. The original nanocondensation apparatus was recently improved with incorporation of an advanced automation module [70], which increased the efficiency of the data acquisition process and enhanced the accuracy of the measurements. To this end, automation hardware and data acquisition boxes were installed in the system, which controlled the opening and closing of the valves and monitored the pressure of the sample holders in real-time.

2.3 Experimental procedure

To prepare the nanocondensation apparatus for the adsorption experiments, an accumulator containing the compressed hydrocarbon mixture was connected to the adsorption inlet valves of the system. Next, the whole instrument was vacuumed for 48 hours to remove any air or humidity from the samples and fluid lines. The temperature of the system was then brought to the experimental condition (i.e., -18 °C) while it was being subjected to a vacuum. The process was stopped once the chamber temperature was stabilized, and a good vacuum condition was observed at the Leybold low-pressure gauge. Subsequently, the adsorption mode was activated on a customized automated LabView software that had been loaded on the computer. In this mode, all Vindum valves that connect the fluid source to the sample holders were opened to allow a gradual injection of fluids into the nanoporous material. During the experiments, the ethane/propane mixture was introduced into the medium in small doses to ensure a slow and consistent buildup of the system pressure. The fluid injection parameters, such as (i) injection time or pulse time and (ii) equilibrium time (i.e., the time difference between two consecutive dosages), were then set on the Labview software (see **Figure A(d)** in Appendix for an illustration of this procedure). The injection time (i.e., dosage time) signifies the duration over which the adsorption valves remain open for the fluid to flow into the material under a certain pressure. The equilibrium time was chosen such that the pressure, after introducing each dose, could reach equilibrium within that time frame. The Rosemount pressure transducers connected to the sample holders recorded the pressure variations in real time. Additionally, a customized Python script plotted this data and facilitated the visual verification of the equilibrium conditions. These two time-related parameters significantly influence the accuracy of the measurements. They can be changed throughout the experiments (as needed) to ensure that a subsequent injection is performed only when the system pressure has attained equilibrium after every dose of fluid is injected. In this work, the initial injection and equilibrium times were fixed at 100 ms and 120 minutes, respectively. The mass and pressure of the sample holders were recorded every second during the adsorption process, and the raw data were logged and plotted throughout the experiment to check for the accuracy. The adsorption isotherm data points, which show mass vs. pressure, were acquired at each equilibrium state (i.e., every two hours). These points were plotted in real-time during the tests to monitor the trend and identify capillary condensation and bulk saturation regions. The adsorption process was stopped once the pressure inside the sample holders reached the bulk saturation pressure of the fluid mixture. Finally, the complete mass-pressure data was processed, and capillary condensation and saturation pressures were determined.

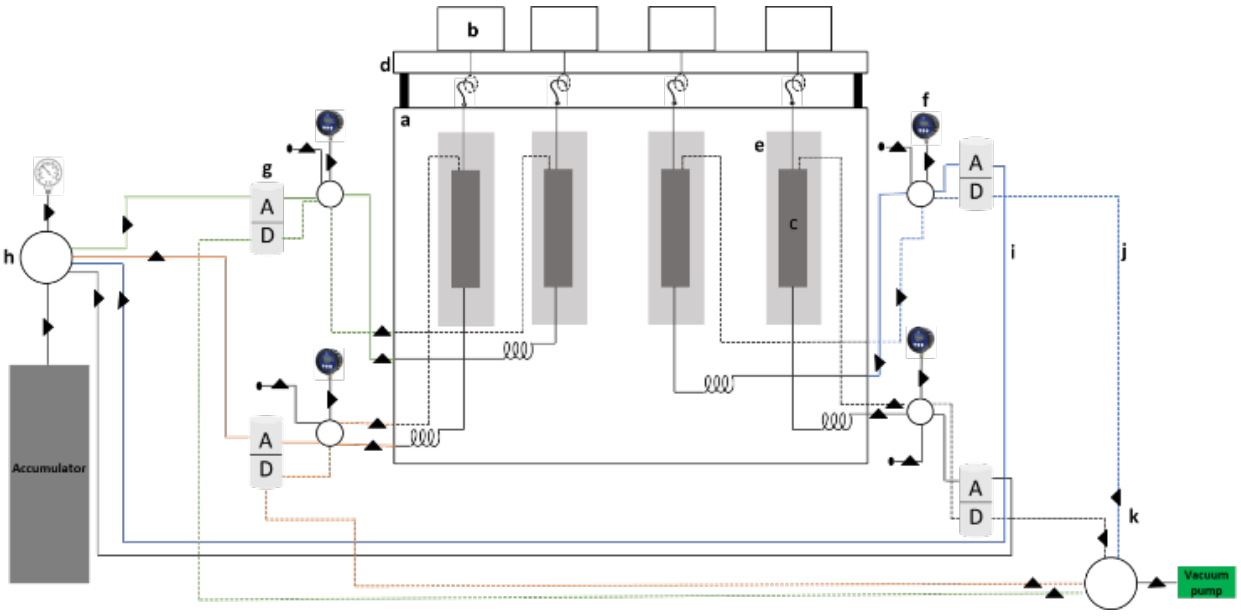

Figure 1. Schematic diagram of the components and configuration of the nanocondensation apparatus: (a) environmental chamber, (b) mass comparator or balance, (c) sample holder, (d) antivibration table, (e) sample holder cover, (f) Rosemount pressure transducers, (g) Vindum valves, (h) manifolds, (i) adsorption fluid lines, and (j) desorption fluid lines.

3 Results and discussion

In this section, we present and discuss the results of the confined phase behavior tests that used ethane/propane mixtures in model nanoporous material MCM-41. We provide the adsorption isotherms for two different ethane/propane mixture compositions in three pore sizes, 7, 10.2, and 12.3 nm, at -18 °C temperature. We calculate the capillary condensation pressures for each pore size by fitting the first derivatives of the mass with respect to pressure (i.e., dm/dP) to a Lorentzian function. The peak of the Lorentzian function indicates the fastest rate of increase in the mass of the adsorbed fluid at a certain pressure and is identified as the capillary condensation pressure [69]. The first inflection point on the adsorption isotherm represents the vapor-liquid phase transition due to nanoconfinement. When the system's pressure is below the saturation pressure of the fluid, an abrupt increase in the adsorbed mass corresponds to the condensation of the fluid inside the nanopores due to enhanced solid-liquid interactions. As the system pressure increases gradually and reaches the bulk saturation pressure, the vapor-liquid phase transition occurs throughout the sample holders and causes a significant increase in the mass of the sample holders. This is identified as a steep increase in the mass on the adsorption isotherms (the vertical-like section of the isotherm), also known as bulk condensation or bubble pressure. Therefore, on an adsorption isotherm, the first inflection point corresponds to the beginning of condensation due to nanopores, and the second abrupt jump in the mass reflects the bulk vapor-liquid phase transition. The bulk vapor-liquid equilibrium (VLE) for various mole fractions of ethane/propane mixture at the experimental temperature of -18 °C is shown in **Figure 2**. The adsorption isotherms for compositions M1 and M2 are presented in **Figures 3** and **4**.

At this temperature, for composition M1, the bulk saturation pressure is expected to be approximately 112 psi (see **Figure 2**). The experimentally measured adsorption isotherms for this mixture are shown in **Figure 3**. The results indicate that the experimental bulk bubble pressure (highlighted by the double-dashed line) for this composition is approximately 94 psi, which is lower than the theoretically calculated bulk bubble pressure highlighted by the single-dashed line. This difference in the saturation pressure of the hydrocarbon mixture can be attributed to the selective adsorption inside the nanopores. The suppression in the saturation pressure indicates higher adsorption of the lighter component, which is ethane in this study. However, more experimental studies are needed to establish and quantify this phenomenon for this mixture. The capillary condensation pressures were calculated for all three pore sizes and are listed in **Table 2**. Additionally, examples of the Lorentzian curve fitting for the dm/dP vs. pressure for both compositions are given in **Figure 5**. It is observed that the effect of nanoconfinement is profound in the smallest pore sizes used here (7 nm), and it decreases with an increase in the pore size. The capillary condensation pressure of ethane/propane mixture for M1 composition in nanopores of 7 nm pore size was measured to be 54.75 psi. However, this pressure increases significantly (73.82 psi) as the pore size scales to 10.2 nm. Furthermore, for the largest pore size used in this study (12.3 nm), a slight increase was observed in the capillary condensation pressure (79.5 psi). This trend is in agreement with those presented in the literature, which shows that the capillary condensation pressure increases with an increase in the pore size. In other words, the degree of suppression of the saturation pressure for vapor-liquid phase transition due to confinement is larger in the tighter nanopores owing to enhanced wall-fluid interactions.

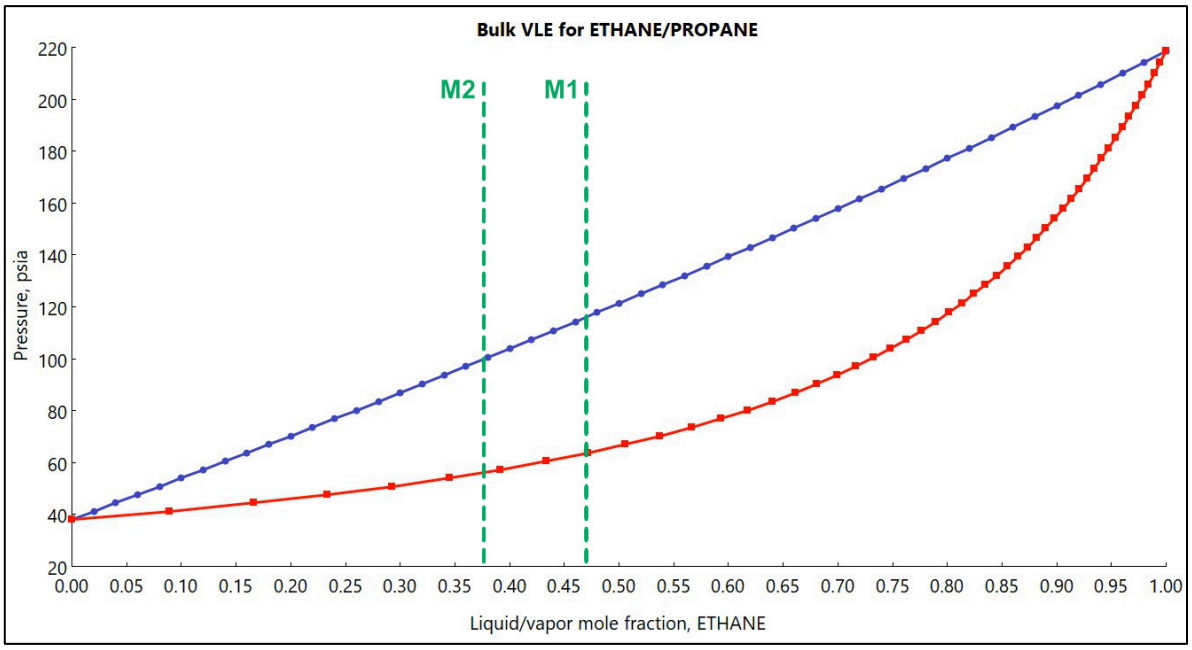

Figure 2. Bulk vapor-liquid equilibrium (VLE) for ethane/propane mixture for various mole fractions of ethane calculated using the Peng-Robinson equation of state. The blue line indicates the bubble point pressure while the orange line shows the dew point pressure.

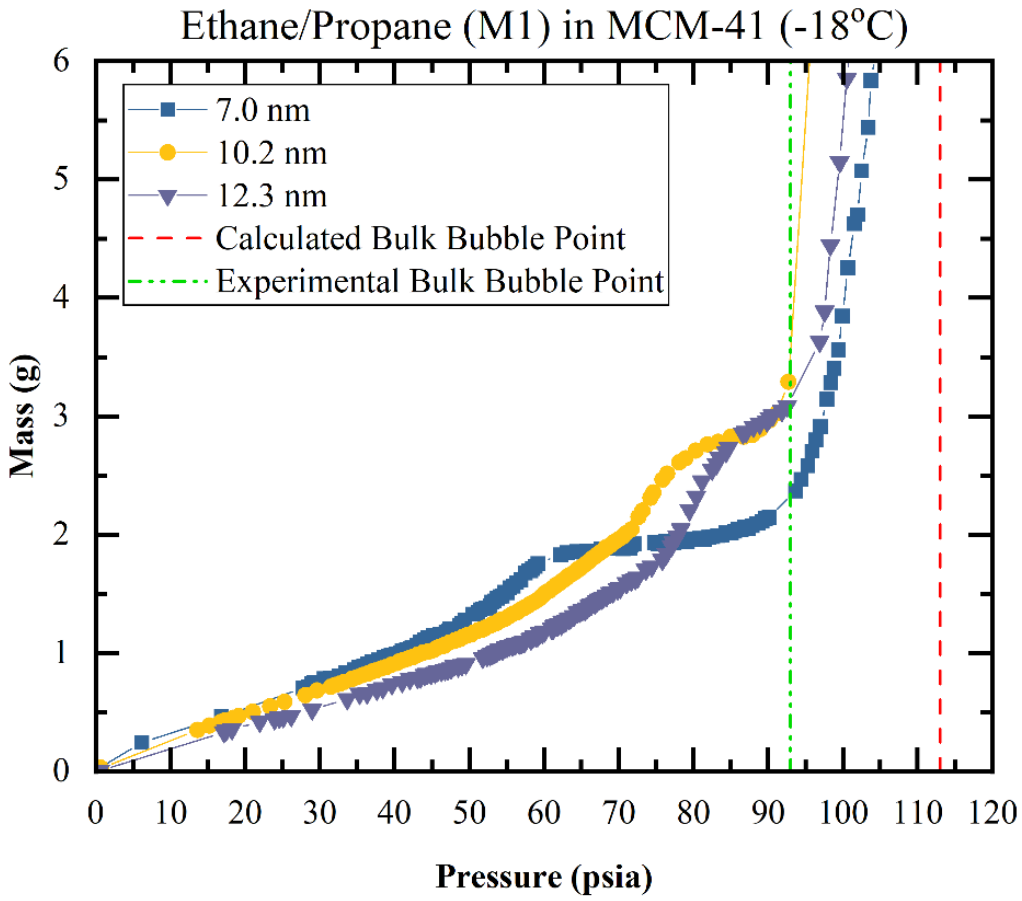

Figure 3. Experimentally measured adsorption isotherms for the mixture M1 (46.6% ethane and 63.4% propane) in MCM-41 of different pore sizes of 7, 10.2, and 12.3 nm at -18 °C. See **Table 1** for the original pore sizes and those calculated using the NLDFT.

The second ethane/propane mixture denoted as M2 was prepared such that the mole fraction of the lighter component (ethane) was lower than that in the first mixture (M1). The M2 mixture contained 37.3 mol% of ethane and 62.7 mol% of propane. This composition included approximately 10 mol% less ethane compared to that in M1, which had 46.6 mol% ethane. The experimentally measured adsorption isotherms for the composition M2 at a similar temperature (-18 °C) are presented in **Figure 4**.

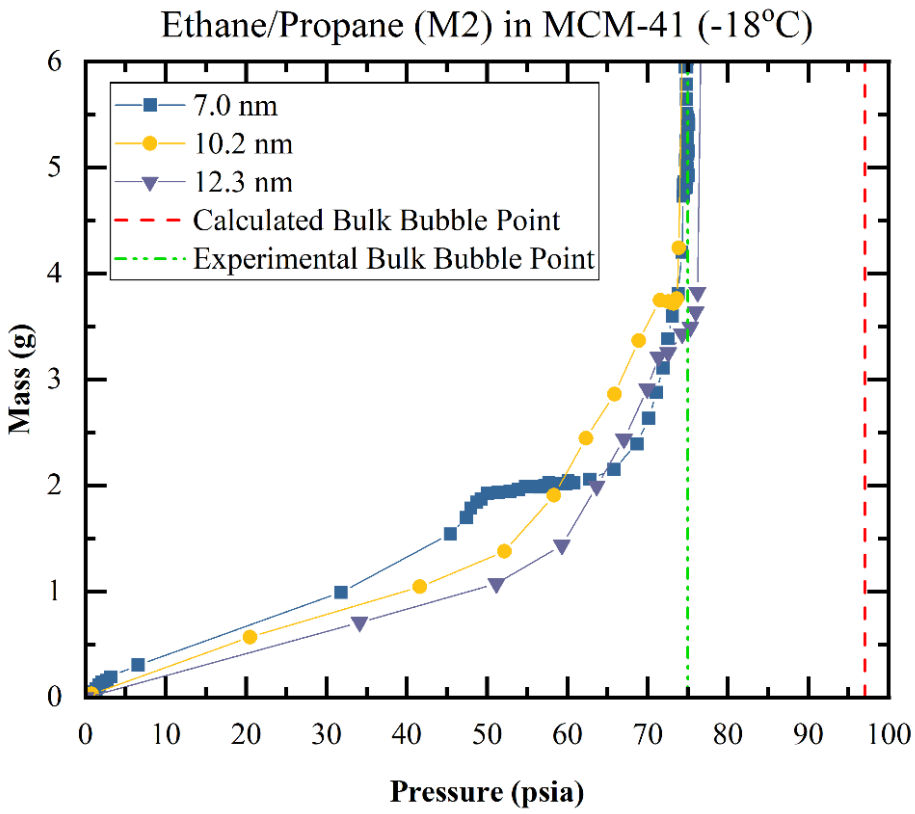

Figure 4. Experimentally measured adsorption isotherms for the composition M2 (37.3% ethane and 62.7% propane) in MCM-41 of different pore sizes (7 nm, 10.2 nm, and 12.3 nm) at -18 °C.

This composition's theoretical bulk saturation pressure is expected to be around 97 psi, which is lower than that of M1 due to less ethane present in the mixture. However, experimentally measured bulk bubble pressure was found to be approximately 75 psi, which is significantly lower than its theoretical counterpart. This again indicates that selective adsorption inside the nanoporous material can cause a decrease in the bulk saturation pressure. In other words, the predominant adsorption of ethane in nanopores compared to propane leaves less ethane in the mixture and changes the composition of the mixture, which results in reduced saturation pressure due to propane's relative heaviness and lower saturation pressure. Similarly, this needs further investigation (proposed later) by performing experiments using compositions with stark differences in the molar fractions. As mentioned earlier, the capillary condensation pressures were calculated from the Lorentzian fits.

An example of the Lorentzian fit of the experimental data for the M2 mixture has been provided in **Figure 5**.

The measured capillary condensation pressures for M2, also provided in **Table 2**, confirm the trends from the experimental results of the M1 mixture. The capillary condensation pressure increases with an increase in the pore size. However, for M2, which has less ethane than mixture M1, the capillary condensation pressures were lower than what was calculated for mixture M1 for all pore sizes. This indicates that the higher is the molar fraction of the lighter component, the lower becomes the adsorption of the heavier component. When the molar fraction of the heavier component increases, the capillary condensation pressures are decreased as the heavy component faces less competition from the lighter one during adsorption. This is supported by the fact that the confinement pressures are not similar for both compositions due to the selective adsorption's dependency on the composition.

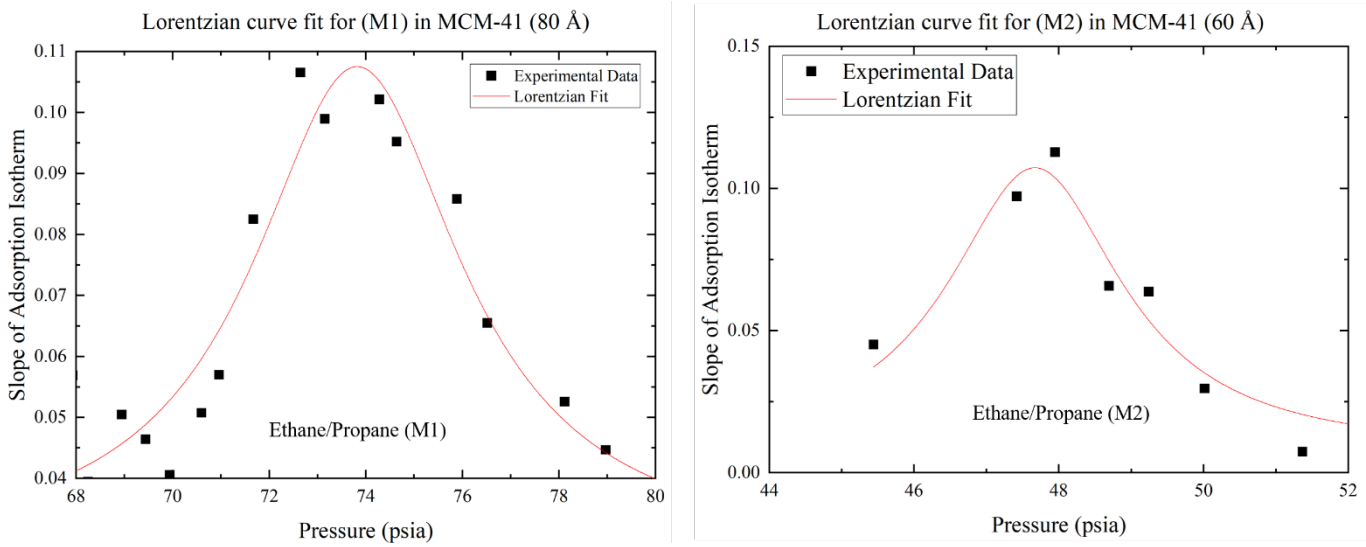

Figure 5. Examples of the Lorentzian curve fit of the first derivative of mass with respect to pressure (i.e., the slope of adsorption isotherm) for ethane/propane mixture of compositions M1 and M2 for two different pore sizes: 80 A (10.2 nm from NLDFT) for M1, and 60 A (7 nm from NLDFT) for M2. The peak of the Lorentzian curve corresponds to the fastest rate of fluid adsorption and is defined as the capillary condensation pressure.

Table 2. Experimentally measured capillary condensation pressures of ethane/propane mixture from the adsorption isotherms for different pore sizes of MCM-41 samples and two different compositions, M1 and M2.

Adsorbent	Temperature (°C)	Mixture	Capillary Condensation Pressure (psia)
MCM-41 (60 Å)	-18	M1	54.75
MCM-41 (80 Å)	-18	M1	73.82
MCM-41 (120 Å)	-18	M1	79.58
MCM-41 (60 Å)	-18	M2	47.67
MCM-41 (80 Å)	-18	M2	62.55
MCM-41 (120 Å)	-18	M2	65.11

Therefore, one may state that the selective adsorption of the hydrocarbon components is relative and is influenced by their molar fractions. Interestingly, the experimentally measured capillary condensation pressures for both compositions conform to the calculated bulk pressures and not the experimental counterparts. It is known from the Young-Laplace equation that the capillary pressure is proportional to the surface tension and inversely related to the pore diameter. Therefore, the capillary pressures may vary linearly with the inverse of the pore size. It is evident from **Figure 6**, which shows the plots of bulk and capillary condensation pressures versus the reciprocal of the pore sizes, that the calculated bulk pressures (representing a pore of infinite diameter) fall on a straight line with capillary condensation pressures, abiding by the Young-Laplace equation.

The diamond symbols in **Figure 6** for both compositions at 0 nm^{-1} correspond to calculated bulk pressures at the inverse of infinite pore diameter. The results strongly agree with the literature and deliver important insights regarding the effect of the composition of the hydrocarbon mixtures on their confined phase behavior. It is indicated that mole percents of either light or heavy components push the occurrence of the confinement-induced phase transitions inside the two-phase region of the mixture. Furthermore, new tests will be conducted using the empty sample holders, i.e., in the absence of nanopores, to determine the experimental bulk saturation pressure of the mixture with different compositions. This will further enrich the inferences drawn from the present results regarding selective adsorption and the shifts in the vapor-liquid phase transition due to confinement.

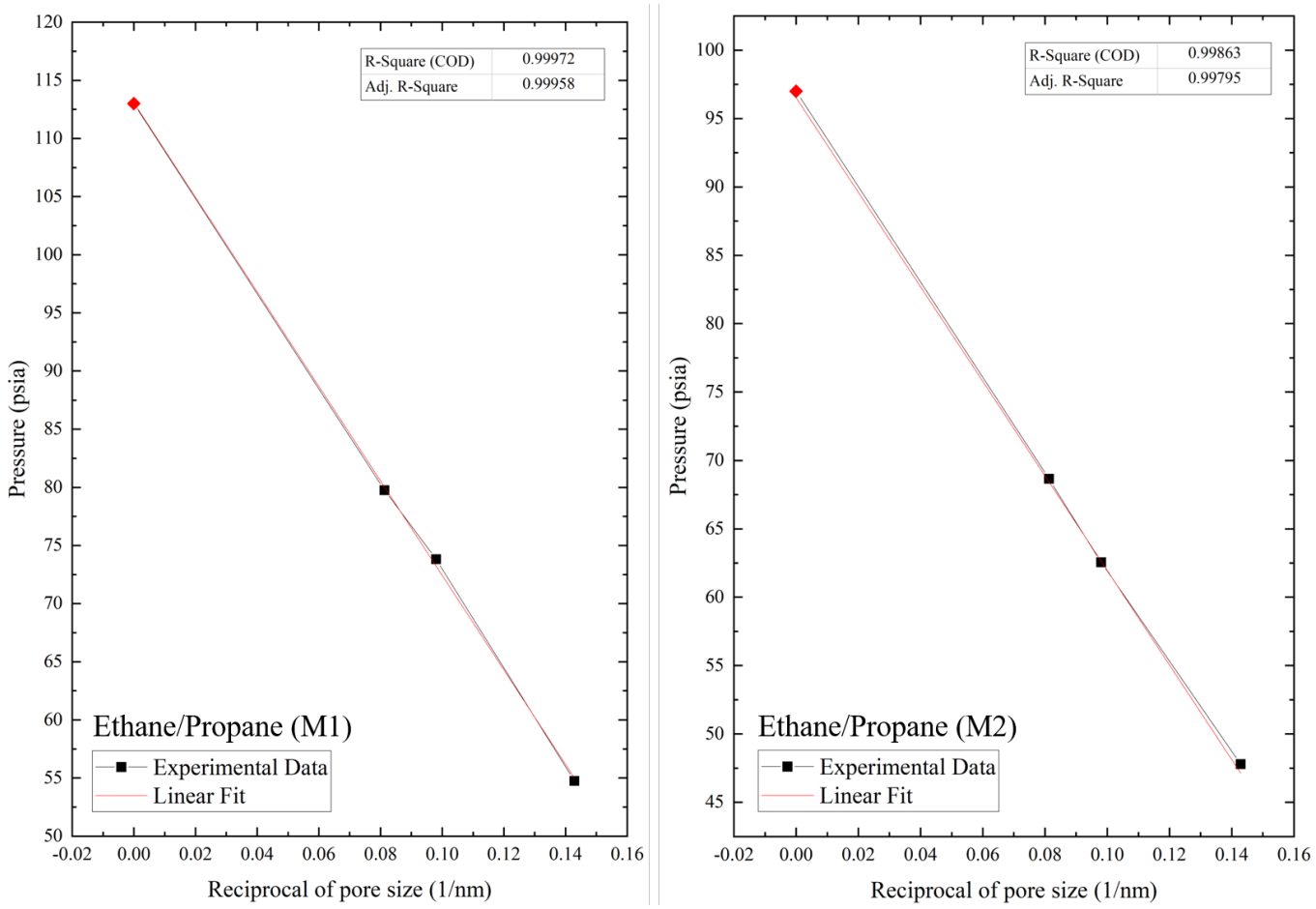

Figure 6. Variation in the experimentally measured capillary condensation pressure with respect to the reciprocal of the pore diameter for both compositions, M1 (left) and M2 (right), of the ethane/propane mixture. The diamond symbol represents the bulk saturation pressure calculated using the PC-SAFT equation of state, and square symbols represent the experimental data of capillary condensation pressure.

4 Conclusions

Ethane and propane are two of the most critical components of typical hydrocarbon mixtures and have numerous applications in several industrial sectors. However, their thermodynamic properties under confinement are still poorly understood and therefore need to be carefully characterized, particularly under mixture conditions. In this study, we experimentally investigated the phase behavior of ethane/propane mixture with different compositions in nanopores of varying pore sizes. To this end, mesoporous material MCM-41 with different pore sizes varying from 7 nm to 12.3 nm was utilized. All experiments were conducted at a temperature of -18 °C. The capillary condensation pressures were calculated from the experimentally measured adsorption isotherms for each composition. The results showed that the confinement effect weakens in larger pores and the vapor-liquid phase transition due to the confinement occurs at much lower pressure in tighter nanopores. In addition, it was also observed that selective adsorption takes place and causes the experimentally measured saturation pressure to be lower than the bulk saturation pressure calculated using an equation of state. It was noticed that the higher mole fraction of the lighter component prohibits the adsorption of the heavier component in the nanopores up to some degree. However, when the mole fraction of the lighter component is decreased, the capillary condensation pressure decreases, and the degree of selective adsorption is also suppressed. The calculated bulk pressure and experimentally measured capillary condensation pressure results showed conformance to the Young-Laplace equation and exhibited a linear proportionality to the reciprocal of the pore size. This confirmed the accuracy of the measurements. A more in-depth investigation is warranted to characterize the relationships between selective adsorption and mole fractions of the lighter and heavier components at different temperature conditions. To this end, new experiments will be conducted for a wide range of temperatures using a mixture of varying compositions. In conclusion, the results from this research enrich the literature with the new experimental data for ethane/propane binary mixtures. In addition, the insights from this work can inform the development decisions made when exploiting unconventional reservoirs in which enormous quantities of hydrocarbons are stored in nanopores. Furthermore, the new results can also facilitate the development of advanced simulation models and rigorous

equations of state that can accurately predict the phase behavior of the confined fluids.

The authors gratefully acknowledge the financial support of Hess Corporation and the University of Wyoming during the course of this research.

References

1. C. Hall, P. Tharakan, J. Hallock, C. Cleveland, and M. Jefferson, “Hydrocarbons and the evolution of human culture,” *NATURE*, vol. 426, pp. 318–322, Nov. 2003.
2. M. Podsiadło, A. Olejniczak, and A. Katrusiak, “Why propane?,” *Journal of Physical Chemistry C*, vol. 117, no. 9, pp. 4759–4763, Mar. 2013.
3. X. Y. Chen, A. Xiao, and D. Rodrigue, “Polymer-based Membranes for Propylene/Propane Separation,” *Separation and Purification Reviews*, vol. 51, no. 1. Taylor and Francis Ltd., pp. 130–142, 2022.
4. A. J. Sundararaj, B. C. Pillai, G. K.R, A. N. Subash, A. P. Haran, and P. Kumar, “Investigation of Ignition Delay for Low Molecular Weight Hydrocarbon Fuel by Using Shock Tube in Reflected Shock Mode,” *Journal of the Geological Society of India*, vol. 93, no. 2, pp. 218–222, Feb. 2019.
5. W. A. Daniel, “Engine Variable Effects on Exhaust Hydrocarbon Composition (A Single-Cylinder Engine Study With Propane as the Fuel),” *SAE Transactions*, vol. 76, pp. 774–795, 1968.
6. K. Andersson, R. Johansson, F. Johnsson, and B. Leckner, “Radiation intensity of propane-fired oxy-fuel flames: Implications for soot formation,” *Energy and Fuels*, vol. 22, no. 3, pp. 1535–1541, May 2008.
7. P. F. Bryan, “Removal of propylene from fuel-grade propane,” *Separation and Purification Reviews*, vol. 33, no. 2. pp. 157–182, 2004.
8. X. Su, F. Zhang, Y. Yin, B. Tu, and M. Cheng, “Thermodynamic analysis and fuel processing strategies for propane-fueled solid oxide fuel cell,” *Energy Conversion and Management*, vol. 204, Jan. 2020.
9. E. Antolini, “Direct propane fuel cells,” *Fuel*, vol. 315., May 01, 2022.
10. M. Aydin *et al.*, “Recent decreases in fossil-fuel emissions of 10. ethane and methane derived from firn air,” *Nature*, vol. 476, no. 7359. pp. 198–201, Aug. 11, 2011.
11. Y. Sawama *et al.*, “Stainless Steel-Mediated Hydrogen Generation from Alkanes and Diethyl Ether and Its Application for Arene Reduction,” *Organic Letters*, vol. 20, no. 10, pp. 2892–2896, May 2018.
12. N. Shah, Y. Wang, D. Panjala, and G. P. Huffman, “Production of hydrogen and carbon nanostructures by non-oxidative catalytic dehydrogenation of ethane and propane,” *Energy and Fuels*, vol. 18, no. 3, pp. 727–735, May 2004.
13. J. P. Cason and C. B. Roberts, “Metallic copper nanoparticle synthesis in AOT reverse micelles in compressed propane and supercritical ethane solutions,” *Journal of Physical Chemistry B*, vol. 104, no. 6, pp. 1217–1221, Feb. 2000.
14. H. Sun, H. Zhu, F. Liu, and H. Ding, “Simulation and optimization of a novel Rankine power cycle for recovering cold energy from liquefied natural gas using a mixed working fluid,” *Energy*, vol. 70, pp. 317–324, Jun. 2014.
15. B. Zühlsdorf, J. K. Jensen, S. Cignitti, C. Madsen, and B. Elmegaard, “Analysis of temperature glide matching of heat pumps with zeotropic working fluid mixtures for different temperature glides,” *Energy*, vol. 153, pp. 650–660, Jun. 2018.
16. S. Douvartzides and I. Karmalis, “Working fluid selection for the Organic Rankine Cycle (ORC) exhaust heat recovery of an internal combustion engine power plant,” in *IOP Conference Series: Materials Science and Engineering*, vol. 161, no. 1, Dec. 2016.
17. O. Demoulin, B. le Clef, M. Navez, and P. Ruiz, “Combustion of methane, ethane and propane and of mixtures of methane with ethane or propane on Pd/γ-Al2O3 catalysts,” *Applied Catalysis A: General*, vol. 344, no. 1–2, pp. 1–9, Jul. 2008.
18. M. Benedict, G. B. Webb, and L. C. Rubin, “An empirical equation for thermodynamic properties of light hydrocarbons and their mixtures. I. Methane, ethane, propane and n-butane,” *The Journal of Chemical Physics*, vol. 8, no. 4, pp. 334–345, 1940.
19. K. S. Pitzer, “Thermodynamics of gaseous hydrocarbons: Ethane, ethylene, propane, propylene, n-butane, isobutane, 1-butene, cis and trans 2-butenes, isobutene, and neopentane (Tetramethylmethane),” *The Journal of Chemical Physics*, vol. 5, no. 6, pp. 473–479, 1937.
20. X. Cao *et al.*, “Phase diagrams for clathrate hydrates of methane, ethane, and propane from first-principles thermodynamics,” *Physical Chemistry Chemical Physics*, vol. 18, no. 4, pp. 3272–3279, Jan. 2016.
21. H. Tanaka, “The thermodynamic stability of clathrate hydrate. III. Accommodation of nonspherical propane and ethane molecules,” *The Journal of Chemical Physics*, vol. 101, no. 12, pp. 10833–10842, 1994.
22. K. S. Pitzer, “The molecular structure and thermodynamics of propane: The vibration frequencies, barrier to internal rotation, entropy, and heat capacity,” *The Journal of Chemical Physics*, vol. 12, no. 7, pp. 310–314, 1944.
23. A. H. Mohammadi, W. Afzal, and D. Richon, “Experimental data and predictions of dissociation conditions for ethane and propane simple hydrates in the presence of distilled water and methane, ethane, propane, and carbon dioxide simple hydrates in the presence of ethanol aqueous solutions,” *Journal of Chemical and Engineering Data*, vol. 53, no. 1, pp. 73–76, Jan. 2008.

24. A. H. Mohammadi, W. Afzal, and D. Richon, "Gas hydrates of methane, ethane, propane, and carbon dioxide in the presence of single NaCl, KCl, and CaCl2 aqueous solutions: Experimental measurements and predictions of dissociation conditions," *Journal of Chemical Thermodynamics*, vol. 40, no. 12, pp. 1693–1697, Dec. 2008.

25. E. W. Lemmon, R. T. Jacobsen, "A Generalized Model for the Thermodynamic Properties of Mixtures," *International Journal of Thermophysics*, vol. 20, pp. 825–835, 1999.

26. J. Gregorowicz, "Solid-fluid phase behaviour of linear polyethylene solutions in propane, ethane and ethylene at high pressures," *Journal of Supercritical Fluids*, vol. 43, no. 2, pp. 357–366, Dec. 2007.

27. L. Djordjevich, R. A. Budenholzer, "Vapor-Liquid Equilibrium Data for Ethane-Propane System at Low Temperatures," *Journal of Chemical & Engineering Data*, vol. 15, no. 1, pp. 10-12, 1970.

28. J. B. Ott, P. R. Brown, and J. T. Sipowska, "Comparison of excess molar enthalpies and excess molar volumes as a function of temperature and pressure for mixtures of (ethane, propane, and butane) with (methanol, ethanol, propan-1-ol, and butan-1-ol)," *The Journal of Chemical Thermodynamics*, vol. 28, pp. 379-404, 1996.

29. I. M. Abdulagatov, S. B. Kiselev, L. N. Levina, Z. R. Zakaryaev, and O. N. Mamchenkova, "Experimental and Theoretical Studies of the Crossover Behavior of the Specific Heat $C_{v,x}$ of Ethane, Propane, and Their Mixture at Critical Isochores," *International Journal of Thermophysics*, vol. 17, pp. 423-440, 1996.

30. J. Chao, R. C. Wilhoit, and B. J. Zwolinski, "Ideal Gas Thermodynamic Properties of Ethane and Propane," *Journal of Physical and Chemical Reference Data*, vol. 2, no. 2, pp. 427–438, 1973.

31. E. J. M. Filipe *et al.*, "Thermodynamics of liquid mixtures of xenon with alkanes: (Xenon + ethane) and (xenon + propane)," *Journal of Physical Chemistry B*, vol. 104, no. 6, pp. 1315–1321, Feb. 2000.

32. R. B. Williams, and D. L. Katz, "Vapor-Liquid Equilibria in Binary Systems. Hydrogen with Ethylene, Ethane, Propylene, and Propane," *Industrial & Engineering Chemistry*, vol. 46, no. 12, pp. 2512-2520, 1954.

33. L. Lue, and D. Blankschtein, "Liquid-State Theory of Hydrocarbon-Water Systems: Application to Methane, Ethane, and Propane," T*he Journal of Physical Chemistry*, vol. 96, no. 21, pp 8582-8594, 1992.

34. Q. Cui and V. H. Smith, "Analysis of solvation structure and thermodynamics of ethane and propane in water by reference interaction site model theory using all-atom models," *Journal of Chemical Physics*, vol. 115, no. 5, pp. 2228–2236, Aug. 2001.

35. I. Velasco, C. Rivas, J. F. Martínez-López, S. T. Blanco, S. Otín, and M. Artal, "Accurate values of some thermodynamic properties for carbon dioxide, ethane, propane, and some binary mixtures," *Journal of Physical Chemistry B*, vol. 115, no. 25, pp. 8216–8230, Jun. 2011.

36. S. Horstmann, K. Fischer, J. Gmehling, and P. Kólař, "Experimental determination of the critical line for (carbon dioxide + ethane) and calculation of various thermodynamic properties for (carbon dioxide + n-alkane) using the PSRK model," *Journal of Chemical Thermodynamics*, vol. 32, no. 4, pp. 451–464, 2000.

37. K. Yasuda and R. Ohmura, "Phase equilibrium for clathrate hydrates formed with methane, ethane, propane, or carbon dioxide at temperatures below the freezing point of water," *Journal of Chemical and Engineering Data*, vol. 53, no. 9, pp. 2182–2188, Sep. 2008.

38. C. B. de la Fuente Juan, D. M. Guillermo, A. B. Esteban, B. B. Susana, "Phase equilibria in binary mixtures of ethane and propane with sunflower oil," *Fluid Phase Equilibria*, vol. 101, pp. 247-257, 1994.

39. Y. Dini, M. Becerra, and J. M. Shaw, "Phase behavior and thermophysical properties of peace river bitumen + propane mixtures from 303 K to 393 K," *Journal of Chemical and Engineering Data*, vol. 61, no. 8, pp. 2659–2668, Aug. 2016.

40. G. W. Billman, B. H. Sage, and W. N. Lacey, "Phase Behavior in the Methane-ethane-n-pentane System," *Trans*, vol. 174, no. 1, pp. 13-24, 1948.

41. H. C. Wiese, H. H. Reamer, and B. H. Sage, "Phase Equilibriums in Hydrocarbon Systems. Phase Behavior in the Methane-Propane-n-Decane System," *Journal of Chemical & Engineering Data*, vol. 15, no. 1, pp. 75-82, 1970.

42. N. G. Tassin, V. A. Mascietti, and M. Cismondi, "Phase behavior of multicomponent alkane mixtures and evaluation of predictive capacity for the PR and RKPR EoS's," *Fluid Phase Equilibria*, vol. 480, pp. 53–65, Jan. 2019.

43. M. Benedict, G. B. Webb, and L. C. Rubin, "An empirical equation for thermodynamic properties of light hydrocarbons and their mixtures: II. Mixtures of methane, ethane, propane, and n-butane," *The Journal of Chemical Physics*, vol. 10, no. 12, pp. 747–758, 1942.

44. J. Vairogs, A. J. Klekers, and W. C. Edmister, "Phase Equilibria in the Methane-Ethane-Propane-n-Pentane-n-Hexane-n-Decane System," *AIChE Journal*, vol. 17, no. 2, pp. 308-312, 1971.

45. A. R. Price and R. Kobayashi, "Low Temperature Vapor-Liquid Equilibrium in Light Hydrocarbon Mixtures: Methane-Ethane-Propane System," *Journal of Chemical & Engineering Data*, vol. 4, no. 1, pp. 40-52, 1959.

46. E. Lowry and M. Piri, "Effect of Surface Chemistry on Confined Phase Behavior in Nanoporous Media: An Experimental and Molecular Modeling Study," *Langmuir*, vol. 34, no. 32, pp. 9349–9358, Aug. 2018.

47. P. H. Nelson, "Pore-throat sizes in sandstones, tight sandstones, and shales," *AAPG Bulletin*, vol. 93, no. 3, pp. 329–340, 2009.

48. D. R. Cole, S. Ok, A. Striolo, and A. Phan, "Hydrocarbon behavior at nanoscale interfaces," *Reviews in Mineralogy and Geochemistry*, vol. 75, pp. 495–545, 2013.

49. M. Hirscher, B. Panella, and B. Schmitz, "Metal-organic frameworks for hydrogen storage," *Microporous and Mesoporous Materials*, vol. 129, no. 3, pp. 335–339, Apr. 2010.

50. J. Li *et al.*, "Hypercrosslinked organic polymer based carbonaceous catalytic materials: Sulfonic acid functionality and nano-confinement effect," *Applied Catalysis B: Environmental*, vol. 176–177, pp. 718–730, Oct. 2015.

51. H. W. Hu, G. H. Tang, and D. Niu, "Wettability modified nanoporous ceramic membrane for simultaneous residual heat and condensate recovery," *Scientific Reports*, vol. 6, Jun. 2016.

52. M. M. Awad, A. S. Dalkiliç, and S. Wongwises, "A critical review on condensation heat transfer in microchannels and minichannels," *Journal of Nanotechnology in Engineering and Medicine*, vol. 5, no. 1, 2014.

53. S. Zarei, H. R. Talesh Bahrami, and H. Saffari, "Effects of geometry and dimension of micro/nano-structures on the heat transfer in dropwise condensation: A theoretical study," *Applied Thermal Engineering*, vol. 137, pp. 440–450, Jun. 2018.

54. M. Thommes and K. A. Cychosz, "Physical adsorption characterization of nanoporous materials: Progress and challenges," *Adsorption*, vol. 20, no. 2–3, pp. 233–250, Feb. 2014.

55. Y. Zhao and Z. Jin, "Hydrocarbon mixture phase behavior in multi-scale systems in relation to shale oil recovery: The effect of pore size distributions," *Fuel*, vol. 291, May 2021.

56. E. Barsotti, S. P. Tan, S. Saraji, M. Piri, and J. H. Chen, "A review on capillary condensation in nanoporous media: Implications for hydrocarbon recovery from tight reservoirs," *Fuel*, vol. 184. Elsevier Ltd, pp. 344–361, Nov. 15, 2016.

57. E. Barsotti, "Capillary Condensation in Shale: A Narrative Review," in *SPE Annual Technical Conference and Exhibition*, SPE-199768-STU, September 2019.

58. X. Dong, H. Liu, W. Guo, J. Hou, Z. Chen, and K. Wu, "Study of the confined behavior of hydrocarbons in organic nanopores by the potential theory," *Fluid Phase Equilibria*, vol. 429, pp. 214–226, Dec. 2016.

59. Y. Ma and A. Jamili, "Using Simplified Local Density/ Peng-Robinson Equation of State to Study the Effects of Confinement in Shale Formations on Phase Behavior," SPE-168986-MS 2014.

60. Y. Seo, S. Lee, I. Cha, J. D. Lee, and H. Lee, "Phase equilibria and thermodynamic modeling of ethane and propane hydrates in porous silica gels," *Journal of Physical Chemistry B*, vol. 113, no. 16, pp. 5487–5492, Apr. 2009.

61. S.P. Tan and M. Piri, "Equation-of-State Modeling of Associating-Fluids Phase Equilibria in Nanopores", *Fluid Phase Equilib.,* vol. 405, 157–166, 2015.

62. E. Barsotti, S. P. Tan, M. Piri, and J. H. Chen, "Phenomenological Study of Confined Criticality: Insights from the Capillary Condensation of Propane, n -Butane, and n -Pentane in Nanopores," *Langmuir*, vol. 34, no. 15, pp. 4473–4483, Apr. 2018.

63. E. Barsotti, E. Lowry, M. Piri, and J. H. Chen, "Using Capillary Condensation and Evaporation Isotherms to Investigate Confined Fluid Phase Behavior in Shales," in *E3S Web of Conferences*, vol. 146, Feb. 2020.

64. E. Barsotti, S. P. Tan, M. Piri, and J. H. Chen, "Capillary-condensation hysteresis in naturally-occurring nanoporous media," *Fuel*, vol. 263, Mar. 2020.

65. Y. Zhao and Z. Jin, "Hydrocarbon-phase behaviors in shale nanopore/fracture model: Multiscale, multicomponent, and multiphase," *SPE Journal*, vol. 24, no. 6, pp. 2526–2540, 2019.

66. Y. Zhao, Y. Wang, J. Zhong, Y. Xu, D. Sinton, and Z. Jin, "Bubble Point Pressures of Hydrocarbon Mixtures in Multiscale Volumes from Density Functional Theory," *Langmuir*, vol. 34, no. 46, pp. 14058–14068, Nov. 2018.

67. B. Jin, R. Bi, and H. Nasrabadi, "Molecular simulation of the pore size distribution effect on phase behavior of methane confined in nanopores," *Fluid Phase Equilibria*, vol. 452, pp. 94–102, Nov. 2017.

68. K. Jean Edler, "Template Induction of Supramolecular Structure: Synthesis and Characterisation of the Mesoporous Molecular Sieve, MCM-41," Ph.D. Thesis, 1997.

69. E. Barsotti, S. Saraji, and M. Piri, "Nanocondensation Apparatus", *US Patent*, US*15*/588,094, 2017.

70. R. Alloush, E. Lowry, and M. Piri, "Automated Apparatus for Characterization of Fluid-Solid Systems," *US Patent*, *US63/186,366*, Filed May 10, 2021.

Appendix I

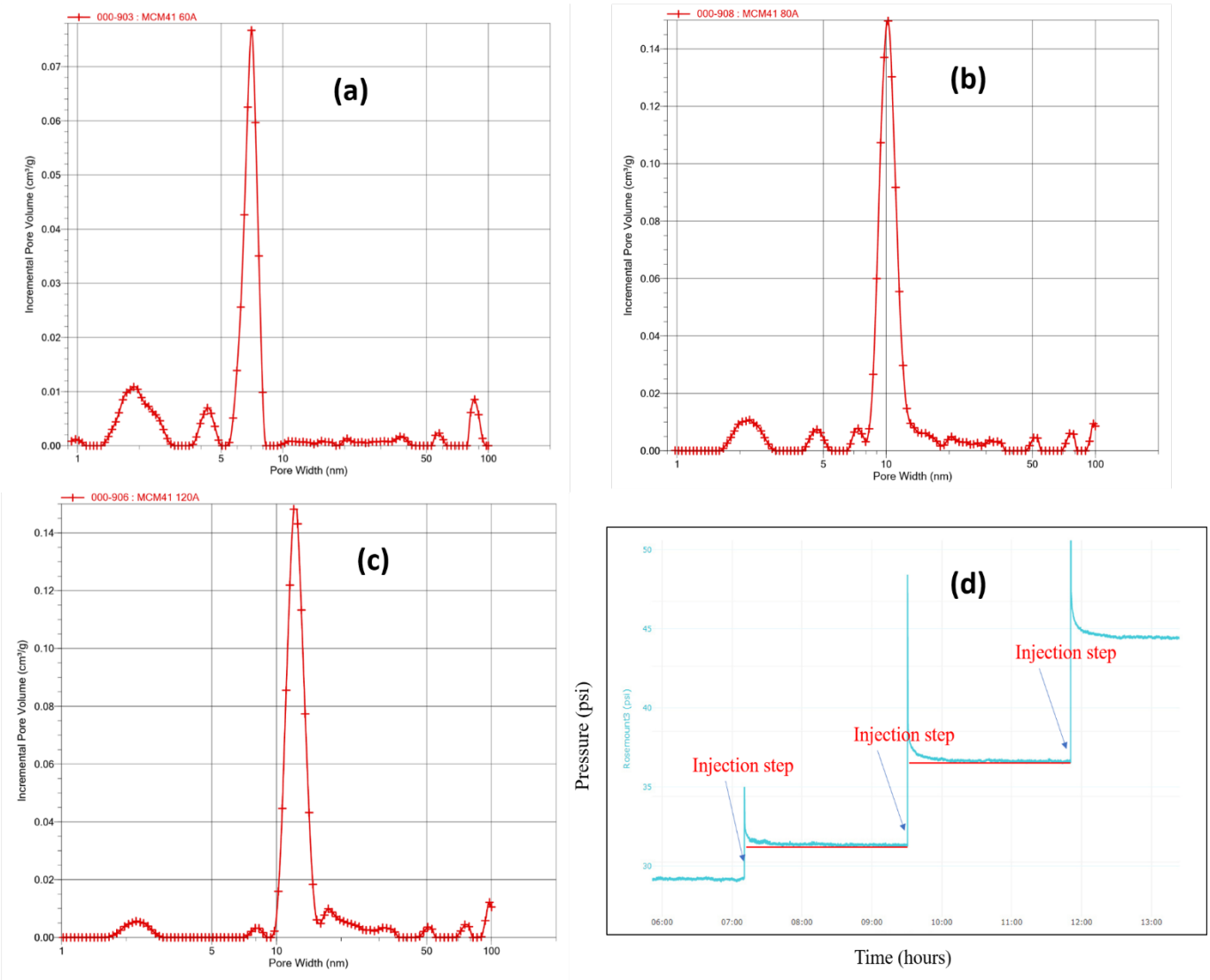

Figure A. (a) – **(c)**: The NLDFT calculated pore size distributions obtained for the MCM-41 samples with pore diameters of 60 Å, 80 Å, and 120Å, respectively. **(d)**: An example from the pressure vs. time raw data for a sample holder packed with MCM-41 material (7 nm NLDFT) exhibiting the establishment of equilibrium conditions after each injection step. The red horizontal lines are reference lines added to show the equilibrium (stabilization of the pressure) occurring within the two hours windows after each dosage of fluid.